CO_2-fueled Non-equilibrium Supramolecular Gels as Gas-Encoded Information Encryption Materials

*Yulian Zhang, Xin Liang, and Qiang Yan**

State Key Laboratory of Molecular Engineering of Polymers, Department of Macromolecular Science, Fudan University, No.220 Handan Road, Shanghai 200433, China.

Corresponding author Email: yanq@fudan.edu.cn

Content

1. Materials, Methods and Synthetic Procedures.

Materials. Two kinds of frustrated Lewis acids, tri(pentafluorophenyl)borane (**TB**) and triphenylborane (**TB^F**), were purchased from Sigma-Aldrich. Four kinds of frustrated Lewis bases (**C$_n$TP**, n = 0, 3, 7 and 11) were synthesized by n-alkyl bromide with different chain lengths and dimesitylphosphorus bromide according to the previous literature with modification [1]. The needed compounds, bromomethane, 1-bromobutane, 1-bromooctane, and 1-bromododecane were purchased from TCI and Adamas-beta. A series of substrates (**S1**-**S12**) were used commercially available products without any further purification. All solvents were reagent grade and were treated from Innovative Technologies Solvent Purification system.

Methods. Nuclear magnetic resonance (NMR) spectroscopy was measured on an AVANCE III HD 400 MHz of Bruker BioSpin International Instrument. Tetramethylsilane (TMS) was utilized as an internal standard, and $CDCl_3$ or d_8-toluene were used as the NMR solvents to probe ^{1}H NMR (400MHz), ^{11}B NMR (128 MHz), ^{31}P NMR (162 MHz) spectra of all the frustrated Lewis acid and base. Electrospray ionization mass spectrometry (ESI-MS) was recorded on a Bruker McriOTOF11 ESI-TOF mass spectrometer equipped with an ESI interface and ion trap analyzer. UV-vis spectroscopy and turbidity test was conducted on an Agilent Cary-60 UV-vis spectrometry using a 1.0 mm cuvette. The spectral change of FLP sols fueled by CO_2 was monitored over time and the optical transmittance of FLP sol samples was probed at the wavelength of 600 nm. Atomic force microscope (AFM) was carried out on a Dimension-ICON Scanning probe Microscope (Bruker, Digital Instrument Co. Ltd.) equipped with a MikroMasch silicon cantilever, NSCII (radius < 10 nm, resonance frequency = 300 kHz, spring constant = 40 N/m) with tapping mode at room temperature. The sol state or gel state of FLP-based co-assemblies were drop casted onto the fresh exfoliated mica and allowed to adsorb for 1 min. After excess solution was wicked off with filter paper and the sample was dried for few hours in vacuum before AFM imaging. Transmission electron microscopy (TEM) was recorded on a FEI Tecnai G2-T20 S-TWIN instrument at 120 kV equipped with an

AMT 16 megapixel in-line CCD camera. The sol or gel state of FLP-based co-assemblies in the absence or presence of CO_2 (10 μL) were taken out at given time and dropped onto a copper grid for 2 min and then blotted with filter paper to remove excess solution followed by drying overnight in vacuum oven before TEM observation. Small-angle X-ray scattering (SAXS) analysis was obtained on the diamond light source beam line I22 in the Shanghai Synchrotron Radiation Facility (SRF). The working voltage and current for the X-ray tube are 45 kV and 0.88 mA, and the wavelength of incident X-ray beam was 0.126 nm. The scattering vector (q) was calibrated using silver behenate with the primary reflection peak at q = 1.067 nm^{-1}. X-ray diffraction (XRD) was conducted using an AXS D8 Advance (Bruker, Germany) diffractometer operated at 1,600 W power (40 kV, 40 mA) using Cu-Kα radiation. The FLP co-assembly samples in powder or xerogel (transient gel at ca. 60 min) were prepared by plunging in liquid nitrogen and drying by the process of lyophilization. The dried samples were then mounted on glass slides for diffraction and 2θ was fixed at 5~50°.

CO_2-fueled gelation. **C_{11}TP** and **TB** as the complementary FLP precursors were dissolved in toluene in glass vial, followed by addition of varying concentrations of **S1** substrate. The final mixture solution was incubated for half an hour with stirring at room temperature. CO_2 gas was applied in the solution through a microflow-pump HRF 1425-580 (PraStar, Praxair Co.) connected to a standard gas cylinder (4 L). This equipment can tune the CO_2 pressure and flow rate to quantify the amount of gas aeration. The gas flow rate can be adjusted from 0.002 to 20 mL/s and the pressure can be adjusted from 0.01 to 10 bar. For the gas-FLP binding, the amount of CO_2 addition was set at the given concentrations (1~4 mM). Gel formation was monitored by inverting the glass vial and the apparent lifetimes of the gel state could be roughly determined.

Rheology measurement. The rheological change of FLP-based transient gel networks over time was monitored in parallel plates using HAAKE Par Rotary Rheometer (HAAKE MARS III) with a 40 mm diameter cross-hatched tool. The frequency sweep experiments were performed as a function of angular frequency (0.1 to 100 Hz) at a fixed strain of 0.1% at given temperature, and the storage moduli (*G′*) and the loss moduli (*G″*) was plotted against time.

Catalytic efficiency analysis. The catalytic ability of transient system was examined by analytical high-performance liquid chromatograph (HPLC) using Waters HPLC system (2535 quaternary pump) with 2489 UV-vis detector, and all compounds involved were separated using a linear gradient eluent toluene : chloroform from 95:5 to 60:40. At a fixed time interval (10 min), aliquots of gel suspension was taken out and injected to HPLC with dilution to in-situ monitor the evolution of the concentration of precursor, substrate and catalytic product. The increase of peak areas of catalytic product, benzo[d]imdiazole-2-carboxylic acid, reflects the catalytic kinetics. Calibration curves for substrate ($\lambda = 220$ nm) and product ($\lambda = 281$ nm) were performed in triplicate in order to quantify the compounds over time.

MD simulation of the packing fashion of co-assemblies. The molecular packing mode of FLP precursor and substrate into fibrillar nanostructure was revealed by molecular dynamics (MD) simulations. The MD simulations employed AMBER force field after the structure optimization using M062x with 6-31g (d,p) basis set implanted in Gaussin09.

Fabrication of time-gated 4D code pattern in solution state. FLP stock solutions were prepared by dissolving FLP precursors (**C_{11}TP** and **TB**, 1 mM) in toluene and added three types of substrates (**S1**, **S8** or **S10**, 1 mM) respectively. Trace amount of pH indicator (bromothymol blue, 1 mg) was added in each mixture solution. Upon introduction of the indicator, the stock solutions turned brilliant blue color because of the weak alkalinity of substrates. Afterwards, the three different types of FLP solutions were dropped into the 96-well plate (12 × 8 units) according to a preset pattern and each well unit contained 0.1 mL solution. Purging or blowing enough CO_2 gas (within 60 s) to the plate in a parallel mode and recording their time-dependent phase transition and concomitant color change. At a certain time window, when the sol in different well unit turned into gel state and its color changed from blue to slight yellow, we could read out the obtained pattern as the code information. Different time windows correspond to the different code pattern, and the correct one can be decrypted only at a specified time.

QR code time-gated encryption in solid state. Printing tests were performed on a Canon inkjet printer (MG2400) and Canon PG-845 FINE cartridge, using paper (4 × 4 cm) without optical brightener. The original three kinds of inks (Cyan, Yellow and Blue) were replaced by our FLP sol inks. The FLP-based inks were the mixture of FLP precursor (**C_{11}TP** and **TB**, 1 mM) and substrate (**S1**, **S8** or **S10,** 1 mM), with trace amount of ferrous ion indicator, respectively. The code information was pre-encoded by FLP array in paper and printed. When exposing the paper to moist CO_2 gas for minutes, the FLP array began to occur transient gelling transition at a certain time window, which make the indicator show blue color. Consequently, the QR code could be seen and we could scan it by a commercially available smartphone APP. In a similar way, different time windows showed different QR codes, and the correct one can be identified only at a specified time.

Synthetic Routes.

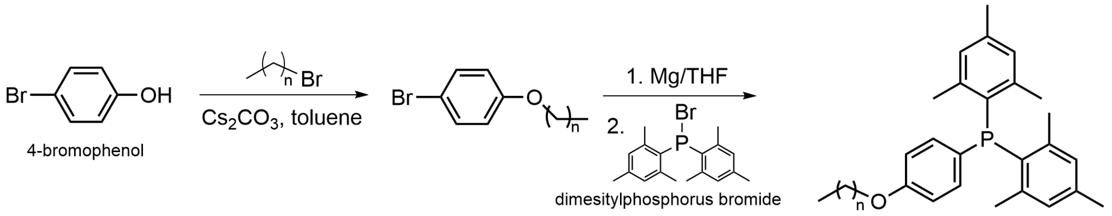

frustrated Lewis base
C$_n$TP, n = 0, 3, 7, 11

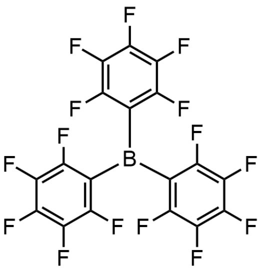

commercially available
frustrated Lewis acid
TB

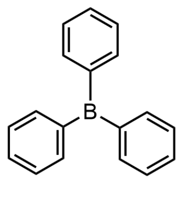

commercially availiable
frustrated Lewis acid
TB^F

Figure S1. Synthetic routes of frustrated Lewis acids (**C$_n$TP**, n = 0, 3, 7 ,11) and their complementary frustrated Lewis bases (**TB** and **TB^F**).

Synthesis of 1-bromo-4-(dodecyloxy)benzene. Typically, 4-bromophenol (8.59 g, 50 mmol) dissolved in 100 mL of toluene was added 1-bromododecane (12.41 g, 50 mmol) and cesium carbonate (1.63 g, 0.1 equiv.). The mixture was reacted at room temperature in the presence of N_2 with stirring overnight, and the solution was filtered by removal of solid salt and the solution was filtered by removal of solid salt and washed by 1M HCl and deionized water for twice. Combining the organic phases and concentrated the solution, the residue was purified by silica gel column chromatography (CH_2Cl_2/n-hexane, 1/5) to afford the 1-bromo-4-(dodecyloxy)benzene intermediate product (12.07 g, yield: 71%). ^{1}H NMR ($CDCl_3$, δ, ppm): 7.40 (d, 2H, $J = 8.4$ Hz), 6.80 (d, 2H, $J = 8.2$ Hz), 4.01 (t, 2H), 1.76 (m, 2H), 1.46 (m, 2H), 1.20-1.41 (br, 16H), 0.89 (t, 2H). ESI-MS (m/z): calcd. For $C_{18}H_{29}BrO$ [M+H$^+$], 340.14; found, 340.29.

Synthesis of dimesitylphosphorus bromide. The dimesitylphosphorus bromide was prepared according to the literature elsewhere [2,3]. 1,2-dibromoethane was added slowly into a mixture of magnesium turnings (3.60 g, 0.15 mol) and anhydrous THF (80 mL). The mixture was stirred for 1 h, then 2-bromomesitylene (19.80 g, 0.10 mol) was added into the mixture slowly, maintaining gentle reflux. After addition, the reaction mixture was refluxed for another 1 h. Then it was returned back to room temperature and stirred for 3 h. The Grignard reagent solution prepared was isolated by cannula filtration. PBr_3 (12.38 g, 0.05 mol) was dissolved in 50 mL anhydrous THF and cooled to -78 °C. The previously prepared Grignard solution was added dropwise at this temperature for half an hour. Then the mixture was elevated to room temperature and reacted overnight. The solvent was removed under reduced pressure, and the product was extracted by cyclohexane (100 mL × 3). After removing the excess solvent, the dimesitylphosphorus bromide product was obtained as a solid powder under vacuum (10.31 g, yield: 59%). ^{1}H NMR ($CDCl_3$, δ, ppm): 6.78 (s, 4H), 2.26 (s, 12H), 2.20 (s, 6H). ^{31}P NMR ($CDCl_3$, δ, ppm): 75.2. ESI-MS (m/z): calcd. For $C_{18}H_{22}PBr$ [M+H$^+$], 349.06; found, 349.31.

Synthesis of Lewis base (C_{11}TP). Under N_2 protection, the fresh Grignard reagent of

1-bromo-4-(dodecyloxy)benzene (3.62 g, 10 mmol) [4] was cannula transferred into THF solution of the resulted dimesitylphosphorus bromide (1.04 g, 3 mmol) at -78 ºC. The mixture was reacted with stirring at this temperature for 2 h, then at 0 ºC for 1 h, and finally at room temperature for another 4 h. Saturated NH_4Cl solution (20 mL) was added to wash the solution. The organic phase was collected and dried over $MgSO_4$. The crude product was purified by silica gel column chromatography (ethyl acetate/n-hexane, 2/1) to afford the **C$_{11}$TP** frustrated Lewis base (0.74 g, yield: 47%). ^{1}H NMR ($CDCl_3$, δ, ppm): 7.36 (dd, 2H, J = 8.2 Hz), 6.91 (dd, 2H, J = 7.8 Hz), 6.78 (d, 4H, J = 8.4 Hz), 4.01 (t, 2H), 2.24 (s, 6H), 2.22 (s, 12H), 1.75 (m, 2H), 1.46 (m, 2H), 1.27-1.43 (brs, 15H), 0.89 (t, 3H). ^{31}P NMR (d_8-toluene, δ, ppm): -24.2. ESI-MS (m/z): calcd. For $C_{36}H_{51}PO$ [M+H$^+$], 530.37; found, 530.91.

Synthesis of other Lewis bases with different alkyl chains. The synthetic procedures of other frustrated Lewis bases are similar to that of **C$_{11}$TP** and their structures are confirmed by ^{1}H NMR, ^{31}P NMR and ESI mass spectroscopy.

C$_7$TP (0.55 g, yield: 41%). ^{1}H NMR ($CDCl_3$, δ, ppm): 7.39 (dd, 2H, J = 8.8 Hz), 6.90 (dd, 2H, J = 8.2 Hz), 6.78 (d, 4H, J = 9.0 Hz), 4.01 (t, 2H), 2.28 (s, 6H), 2.21 (s, 12H), 1.75 (m, 2H), 1.45 (m, 2H), 1.21-1.41 (mbr, 8H), 0.89 (t, 3H). ^{31}P NMR (d_8-toluene, δ, ppm): -22.7. ESI-MS (m/z): calcd. For $C_{32}H_{43}PO$ [M+H$^+$], 474.31; found, 474.61.

C$_3$TP (0.91 g, yield: 54%). ^{1}H NMR ($CDCl_3$, δ, ppm): 7.38 (dd, 2H, J = 8.2 Hz), 6.90 (dd, 2H, J = 8.5 Hz), 6.78 (d, 4H, J = 9.0 Hz), 4.00 (t, 2H), 2.25 (s, 6H), 2.21 (s, 12H), 1.78 (m, 2H), 1.49 (m, 2H), 0.98 (t, 3H). ^{31}P NMR (d_8-toluene, δ, ppm): -21.3. ESI-MS (m/z): calcd. For $C_{28}H_{35}PO$ [M+H$^+$], 418.24; found, 418.13.

C$_0$TP (0.45 g, yield: 39%). ^{1}H NMR ($CDCl_3$, δ, ppm): 7.30 (dd, 2H, J = 10.8 Hz), 6.94 (dd, 2H, J = 9.2 Hz), 6.76 (d, 4H, J = 8.7 Hz), 3.86 (t, 2H), 2.26 (s, 6H), 2.22 (s, 12H). ^{31}P NMR (d_8-toluene, δ, ppm): -20.2. ESI-MS (m/z): calcd. For $C_{25}H_{29}PO$ [M+H$^+$], 376.20; found, 376.41.

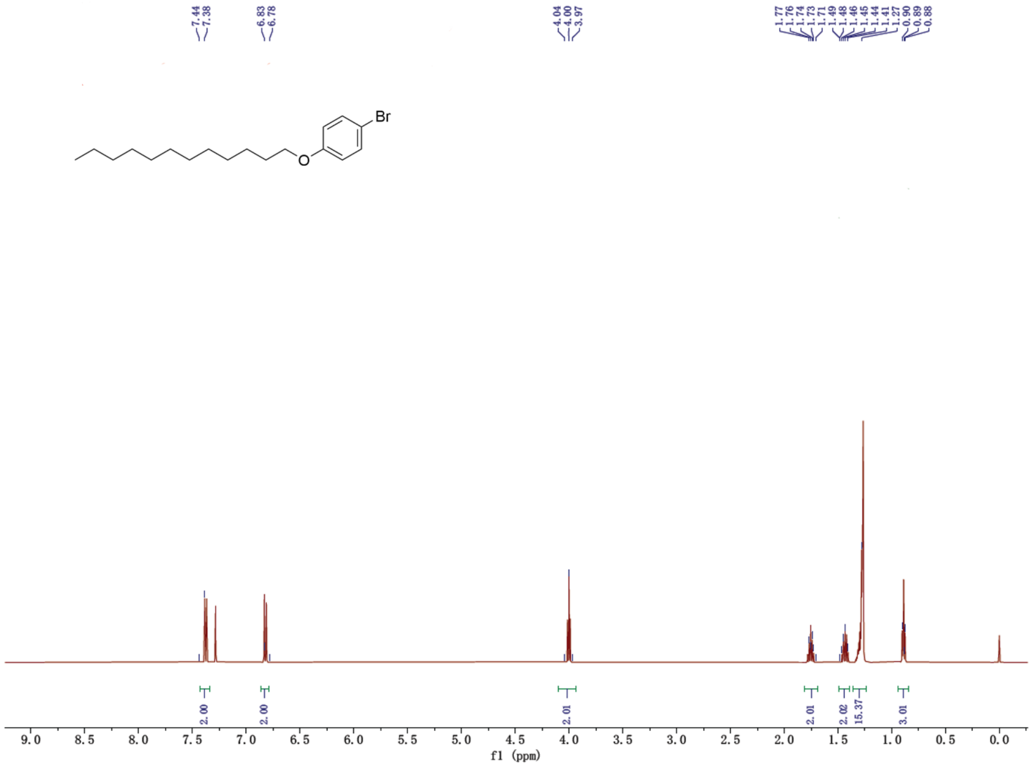

Figure S2. ^{1}H NMR spectrum of 1-bromo-4-(dodecyloxy)benzene ($CDCl_3$).

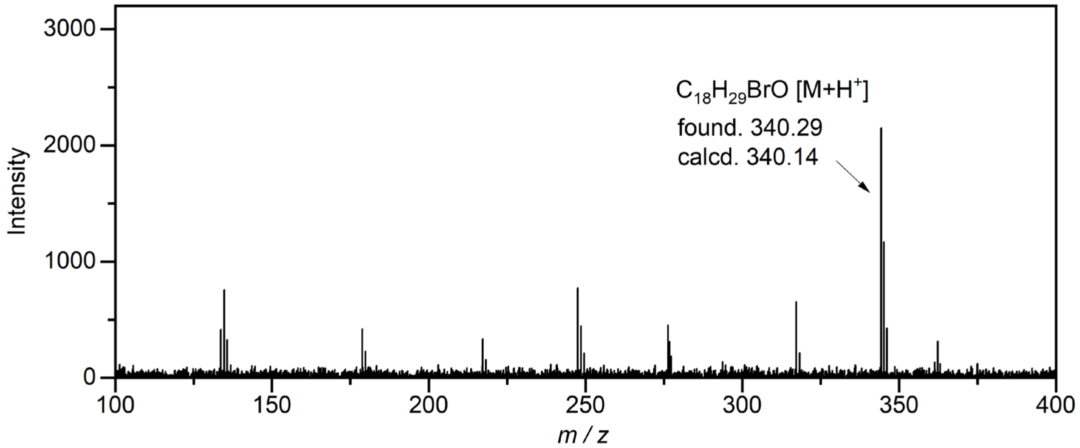

Figure S3. ESI-MS spectrum of 1-bromo-4-(dodecyloxy)benzene ($C_{18}H_{29}BrO$, [M+H$^+$], calcd. 340.14; found. 340.29).

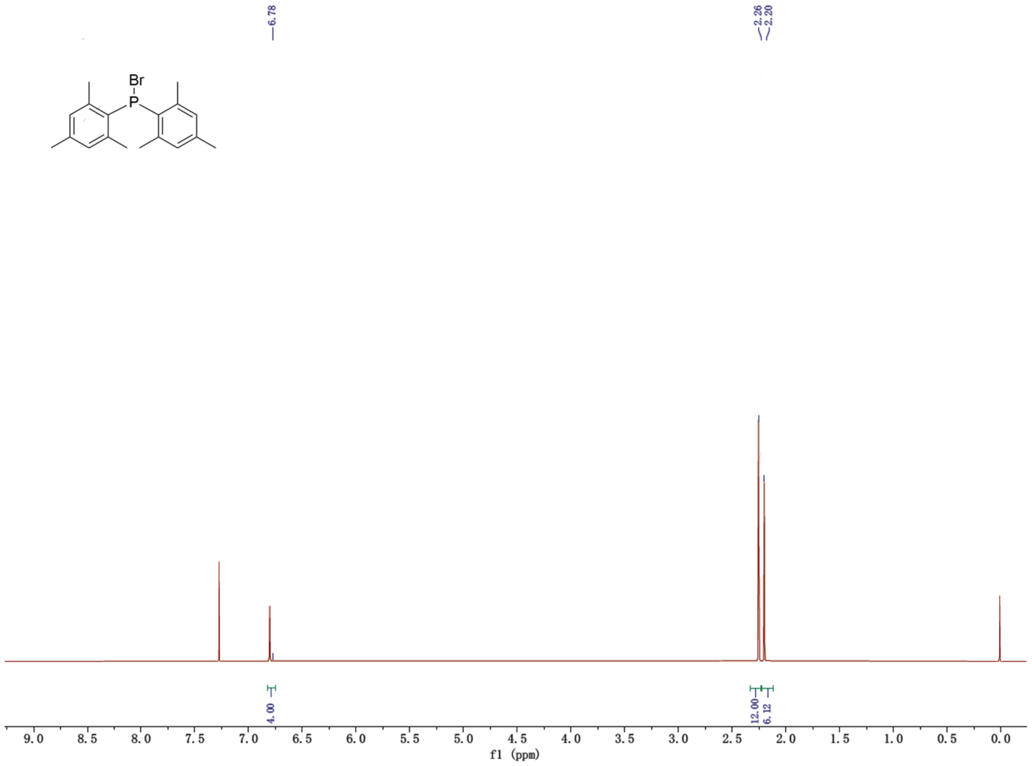

Figure S4. ^{1}H NMR spectrum of dimesitylphosphorus bromide ($CDCl_3$).

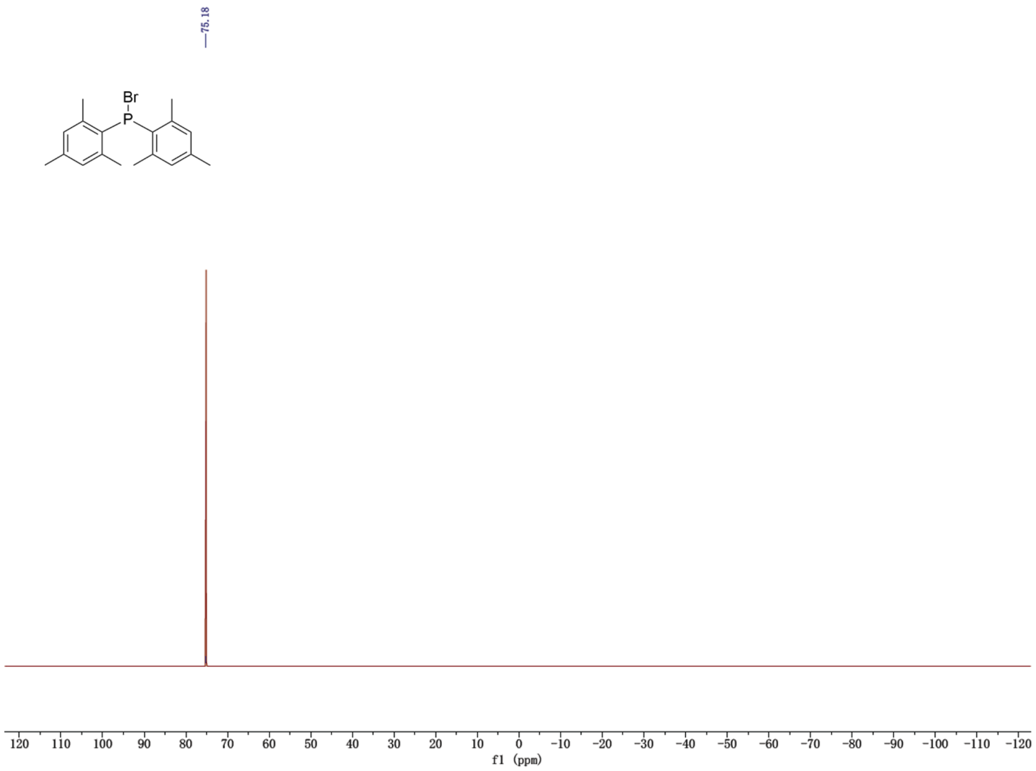

Figure S5. ^{31}P NMR spectrum of dimesitylphosphorus bromide ($CDCl_3$).

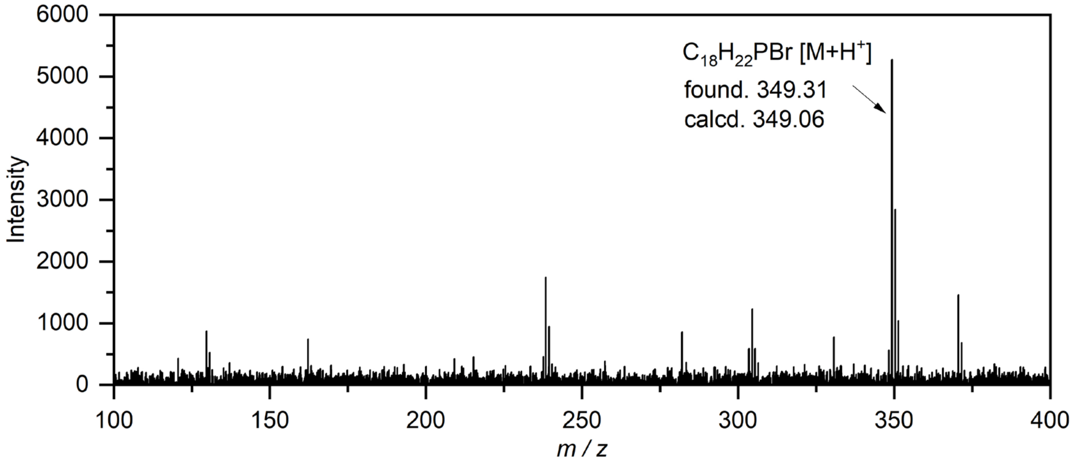

Figure S6. ESI-MS spectrum of dimesitylphosphorus bromide ($C_{18}H_{22}PBr$, [M+H$^+$], calcd. 349.06; found. 349.31).

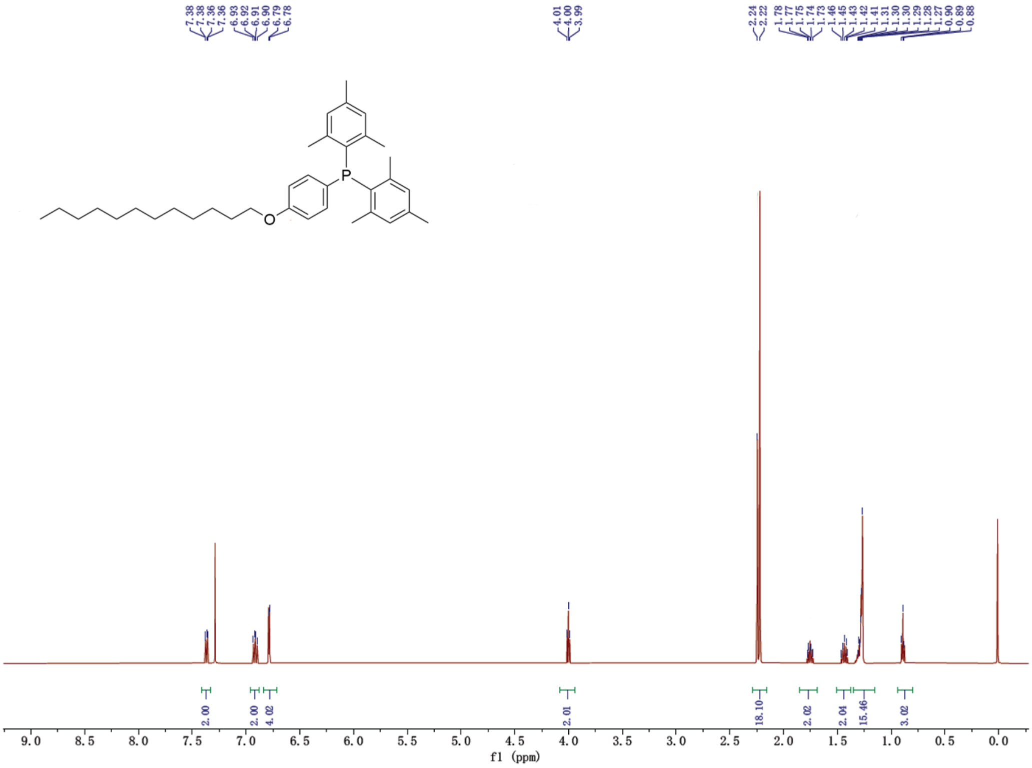

Figure S7. ^{1}H NMR spectrum of frustrated Lewis base, **C$_{11}$TP** (CDCl$_3$).

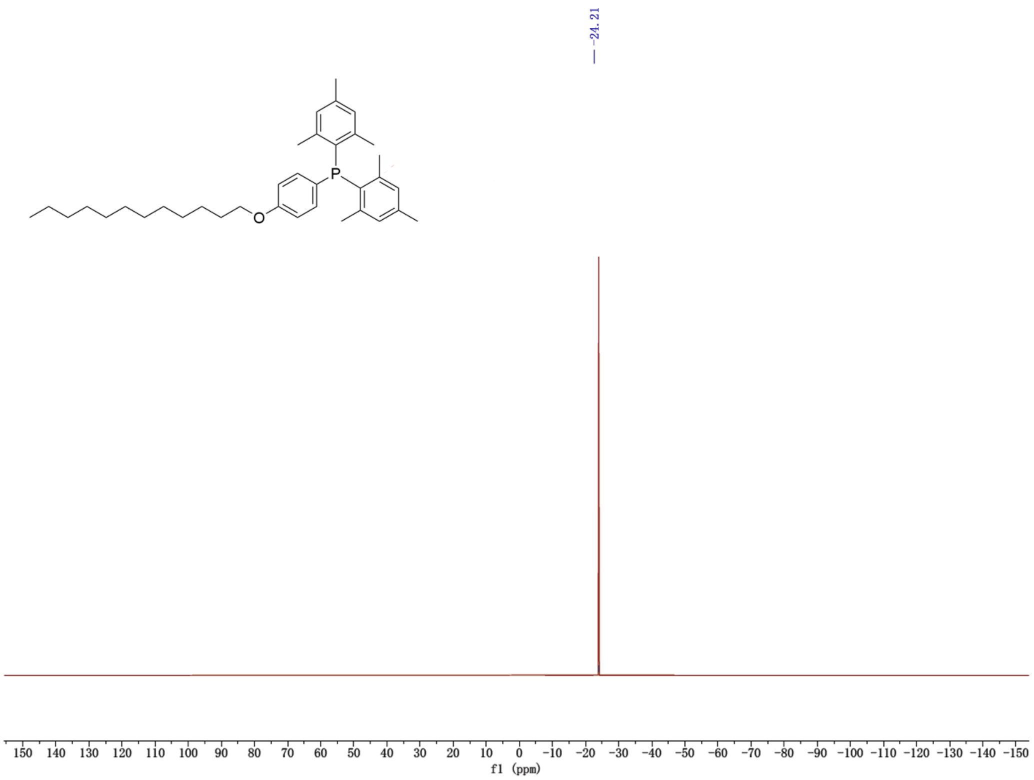

Figure S8. ^{31}P NMR spectrum of frustrated Lewis base, **C$_{11}$TP** (d_8-toluene).

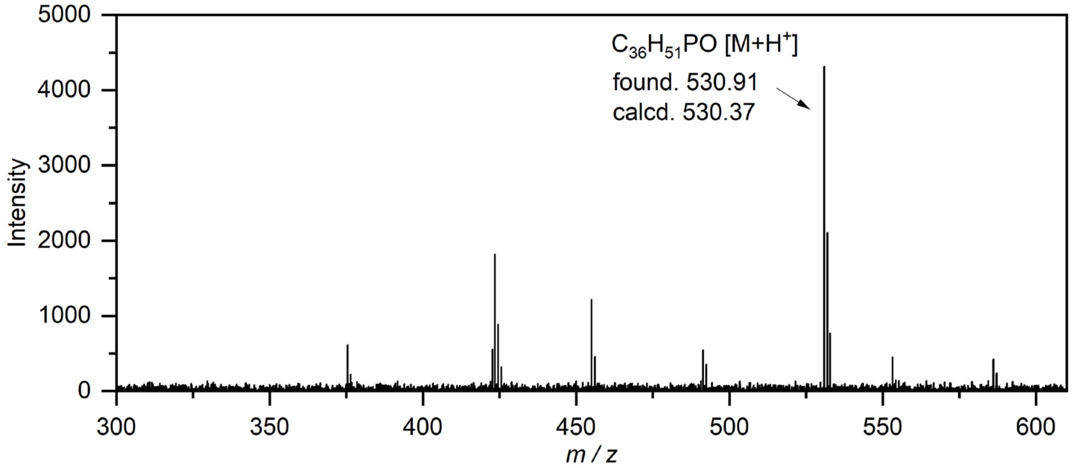

Figure S9. ESI-MS spectrum of frustrated Lewis base, **C$_{11}$TP** ($C_{36}H_{51}PO$, [M+H$^+$], calcd. 530.37; found. 530.91).

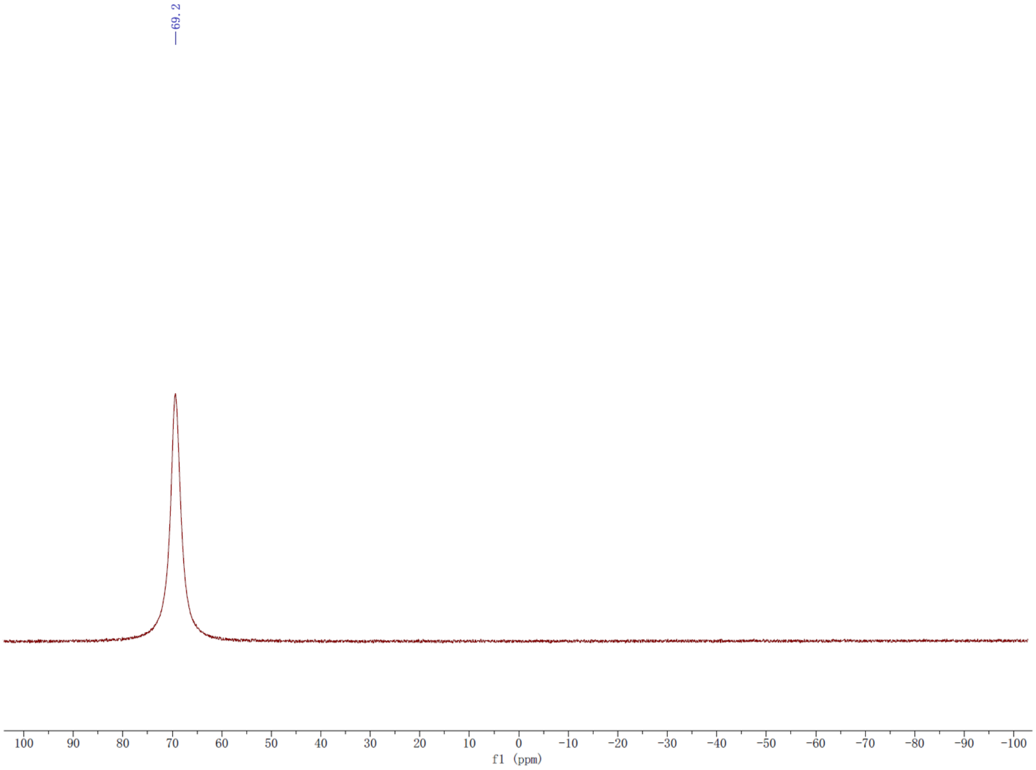

Figure S10. ^{11}B NMR spectrum of frustrated Lewis acid, **TB** (d_8-toluene).

2. Supplementary characterization for CO_2-fueled transient gelation.

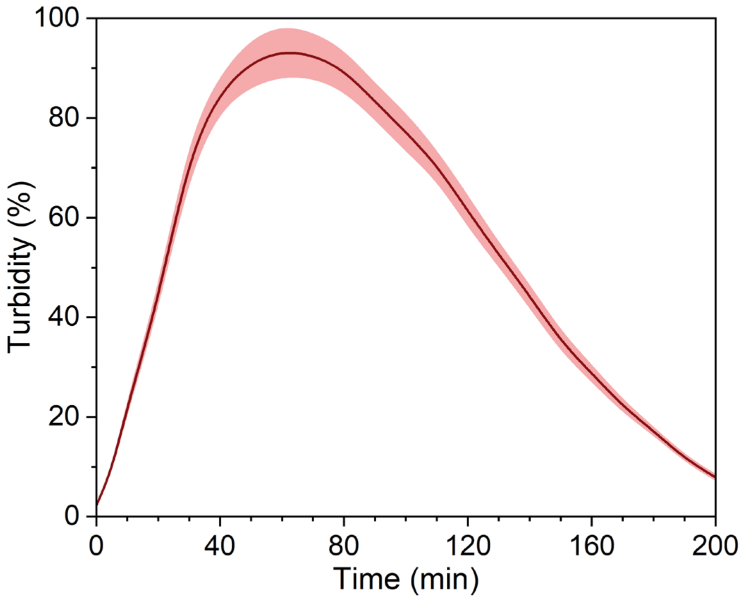

Figure S11. UV-Vis turbidity measurement of **C_{11}TP-TB-S1** mixture in toluene at the wavelength of 600 nm over time after addition of CO_2 gas (1 mM). The concentration of two FLP precursors (**C_{11}TP** and **TB**) were 4 mM and **S1** substrate was at 1 mM.

We used the solution turbidity change of assemblies against time to indicate their phase transition process [5]. The change of solution turbidity showed a parabolic profile, first giving a sharp increase within ~60 min and then decreasing to the initial state within ~200 min. Such a changing trend corresponds to the sol-gel-sol phase transition process.

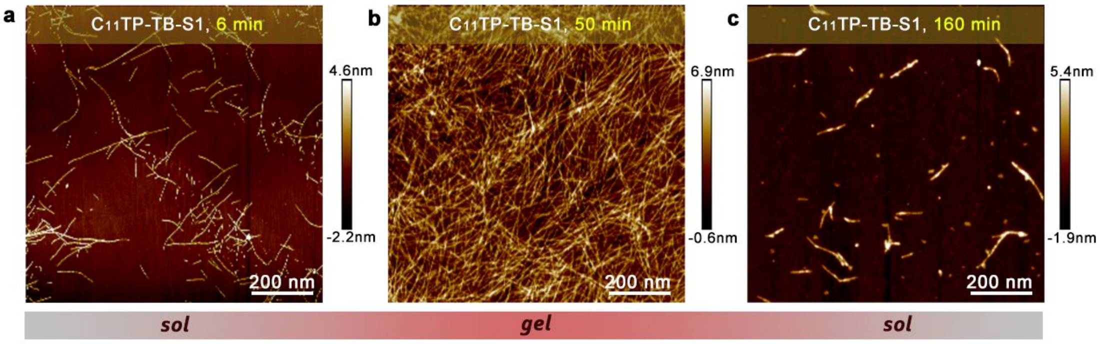

Figure S12. AFM images showing the assembly morphological change of **C_{11}TP-TB-S1** mixture in toluene after addition of CO_2 gas (1 mM): (a) 6 min, (b) 50 min, (c) 160 min.

At the beginning (6 min), we found that the precursors and substrates can form short nanofibrils with homogenous diameter but varying lengths (***Figure S12a***). There were some bundling and entanglement existing among them, which should be the incentive for an uplifted solution viscosity. Over time, these nanofibrils can continue to grow along their 1D axis, and form long fiber network at 50 min. The diameter of these fibers remained constant but their average lengths extended tens of times to several microns. The increasing number of physical crosslinkings and entangled domains among these long fibers resulted in the formation of fibrous gel (***Figure S12b***). However, such gel network can spontanesouly dissociate after 160 min, as indicated by their rupture and cleavage into fragments (***Figure S12c***). This spontaneous morphological evolution in AFM images are consistent with the TEM results.

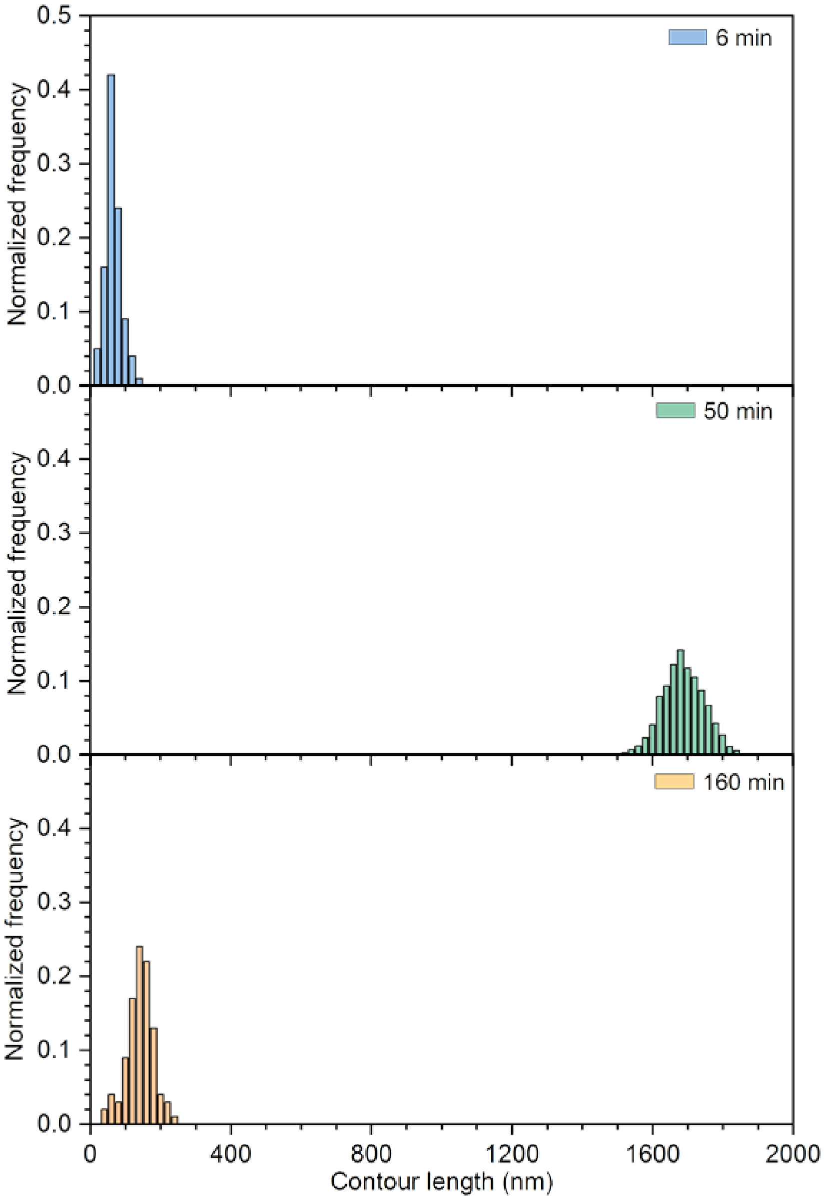

Figure S13. The contour length distribution change of **C$_{11}$TP-TB-S1** fiber assemblies after addition of CO_2 gas (1 mM) at different times: 6 min (upper panel), 50 min (middle panel), and 160 min (bottom panel). Counting over 100 fibers by AFM fiber statistics.

At the beginning (6 min), the contour length of the formed short nanofibrils ranges from 20–150 nm. When these fibrils grew into long nanofiber network, their length increases to several micrometers. After 160 min, the fibers are totally dissociation because their length returns to the initial value (20–220 nm). The auto-statistics of fiber parameters (number, size, diameter, etc.) are finished by FiberApp tool developed by Mezzenga [6].

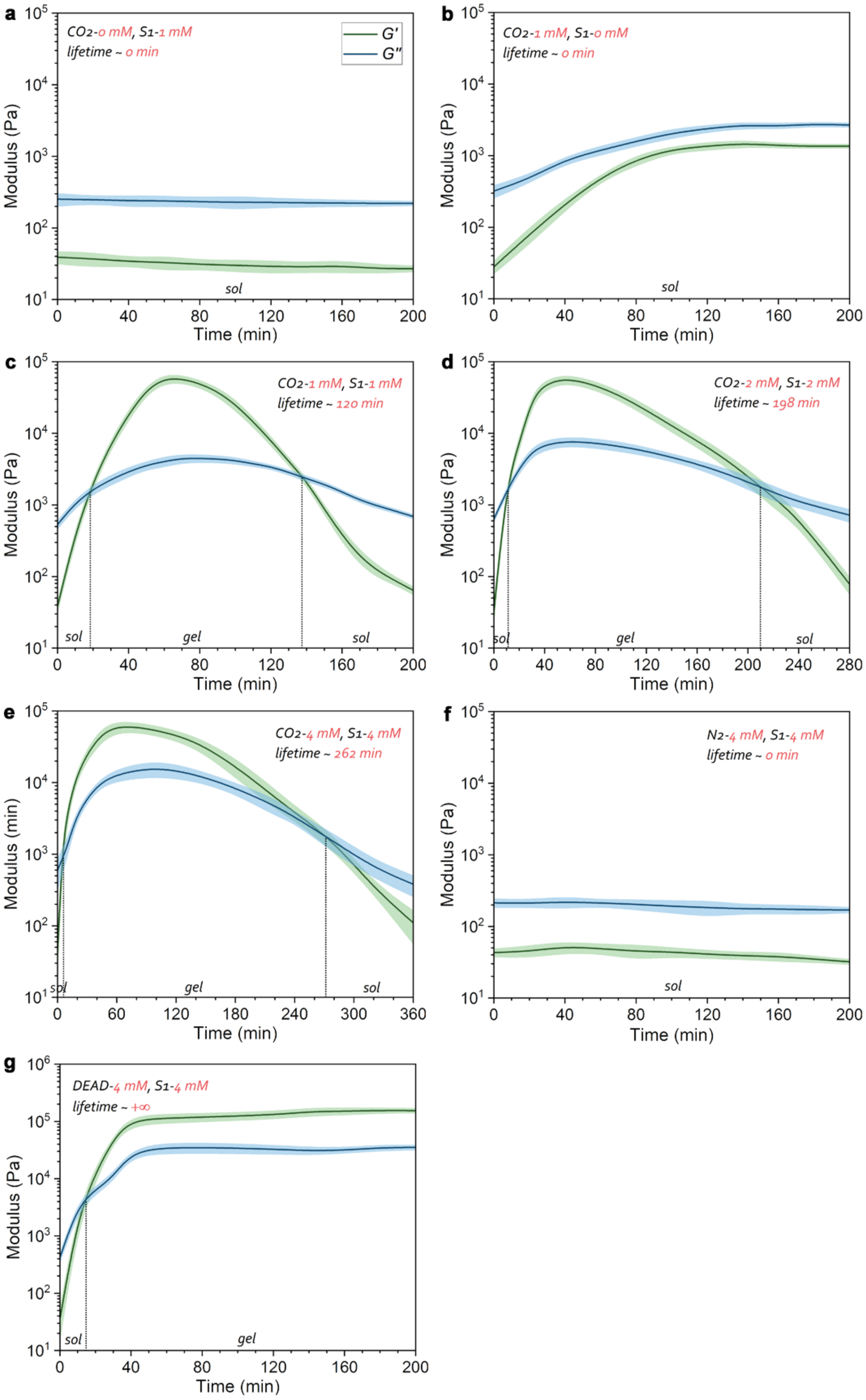
a
CO2-0 mM, S1-1 mM
lifetime ~ 0 min
G′
G″
sol
Modulus (Pa)
Time (min)
b
CO2-1 mM, S1-0 mM
lifetime ~ 0 min
sol
Modulus (Pa)
Time (min)
c
CO2-1 mM, S1-1 mM
lifetime ~ 120 min
sol
gel
sol
Modulus (Pa)
Time (min)
d
CO2-2 mM, S1-2 mM
lifetime ~ 198 min
sol
gel
sol
Modulus (Pa)
Time (min)
e
CO2-4 mM, S1-4 mM
lifetime ~ 262 min
sol
gel
sol
Modulus (min)
Time (min)
f
N2-4 mM, S1-4 mM
lifetime ~ 0 min
sol
Modulus (Pa)
Time (min)
g
DEAD-4 mM, S1-4 mM
lifetime ~ +∞
sol
gel
Modulus (Pa)
Time (min)

Figure S14. Rhelogical change of the transient gelation under various conditions: (a) no CO_2 fuel, (b) no **S1** substrate, (c) 1.0 mM of CO_2 fuel and **S1** substrate, (d) 2.0 mM of CO_2 fuel and **S1** substrate, (e) 4.0 mM of CO_2 fuel and **S1** substrate, (f) using N_2 as gas fuel (4.0 mM) instead of CO_2 with equimolar ratio of **S1** substrate, (g) using DEAD competing binder as fuel instead of CO_2 gas. The concentration of two FLP precursors (**C_{11}TP** and **TB**) were fixed at 4.0 mM in all the tests.

We used rheology method to monitor the sol-gel-sol phase transition over time [7,8]. It can be seen that no gelling phenomenon happened when the system is absent of either CO_2 fuel or substrate (***Figure S14a,b***). This hints that both gas fuel and substrate play crucial role in driving the co-assembly of FLP precursors into gel network. If we varied the concentration of CO_2 fuel and substrate (1.0→4.0 mM), the system showed transient gelation, and moreover, higher level the fuel and substrate applied, longer gel lifetime (120→262 min) and higher modulus (58.2→122.6 kPa) was (***Figure S14c-e***). These mean that more CO_2 cross-linking sites are formed in the network that reinforce their mechanical strength. As control, if we used N_2 as gas fuel to replace CO_2, no gel can produce because N_2 is of chemical inertness incapable of binding to the FLP precursors (***Figure S14f***). In addition, if used DEAD competing binder as fuel to replace CO_2, the gel can rapidly form without spontaneous collapse (***Figure S14g***), because DEAD is of stronger binding affinity with FLP precursors and it has no reactivity with **S1** substrate. This is because that there is no dissipative pathway to deplete the DEAD fuel in the gel system.

3. Supplementary characterization for non-equilibrium co-assembly mechanism.

Kinetic studies of the forward CO_2-binding path and the backward CO_2 debinding path.

In this CO_2-fueled transient gelation system, there are two main processes. The forward pathway is that CO_2 gas dynamically binds to the FLP precursors (**C_{11}TP** and **TB**) and induces the formation of co-assembled gel. Conversely, an underlying reaction as the backward path that induces CO_2 detached from FLP units is responsible to deplete CO_2 fuel and to recover the system. For the forward process, FLP precursors can be bridged by CO_2 to form a dynamic $C_{11}TP–CO_2–TB$ linkage. The associating reaction is as follows,

$$FLP + CO_2 \overset{k_+}{\rightarrow} FLP \cdot CO_2$$

in which the rate coefficient of gas binding reaction can be represented as k_+, and the concentrations of reactant, gas fuel and obtained dative complex are [FLP], $[CO_2]$ and $[FLP \cdot CO_2]$, respectively. Hence, the forward binding rate between FLP precursors and CO_2 fuel can be expressed as Eq. 1.

$$d[FLP]/_{dt} = -k_+[FLP] \cdot [CO_2] \dots \dots \dots \dots (1)$$

While for the backward path, the bound CO_2 species ($C_{11}TP–CO_2–TB$) is catalytically active as the C=O double bond in CO_2 is weakened by this gas bridge. Thus, it can react with the neighboring **S1** substrate through CO_2 insertion and yield a **S1**–COOH product, which can in turn consume CO_2 unit. The backward CO_2 debinding reaction is like that,

$$FLP \cdot CO_2 + S1 \overset{k_-}{\rightarrow} FLP + S1 - COOH$$

If we define the reverse rate coefficient of gas debinding as k-, the backward reaction rate can be expressed as Eq. 2.

$$d[FLP]/_{dt} = k_-[FLP \cdot CO_2] \cdot [S1] \dots \dots \dots \dots (2)$$

Combining the forward and backward reactions, the FLP concentration in solution against reaction time can be expressed as Eq. 3.

$$d[FLP]/_{dt} = -k_+[FLP] \cdot [CO_2] + k_-[FLP \cdot CO_2] \cdot [S1] \dots \dots \dots \dots (3)$$

When the amount of CO_2 gas fuel and the co-assembled substrate are largely excessive to that of FLP precursors, the apparent forward reaction rate, $k_+^{app} = k_+[CO_2]$, whereas the apparent backward reaction rate, $k_-^{app} = k_-[S1]$, are both constant. Hence, Eq. 3. can be simplified as Eq. 4.

$$d[FLP]/_{dt} = -k_+^{app}[FLP] + k_-^{app}[FLP \cdot CO_2] \ldots\ldots\ldots\ldots (4)$$

Since the total concentration of FLP is preset as a constant C_0, thus the sum of free FLP species and gas-bound FLP species is equal to C_0 at any time, that is,

$$C_0 = [FLP] + [FLP \cdot CO_2] \ldots\ldots\ldots\ldots (5)$$

Hence, combining Eq. 4 and Eq. 5, the FLP concentration against time can be given as Eq. 6,

$$d[FLP]/_{dt} = -k_+^{app}[FLP] + k_-^{app}(C_0 - [FLP]) \ldots\ldots\ldots\ldots (6)$$

According to Eq. 6, we could obtain the apparent forward and backward reaction rates (k_+^{app} and k_-^{app}) through monitoring the spectrometric change of FLP species ($\lambda = 266$ nm) by UV-Vis spectroscopy. This kinetic divergency between k_+^{app} and k_-^{app} is the basis to establish a gas-driven dissipative cycle. The variation of UV-Vis absorption intensity of FLP species was shown as ***Figure S15***.

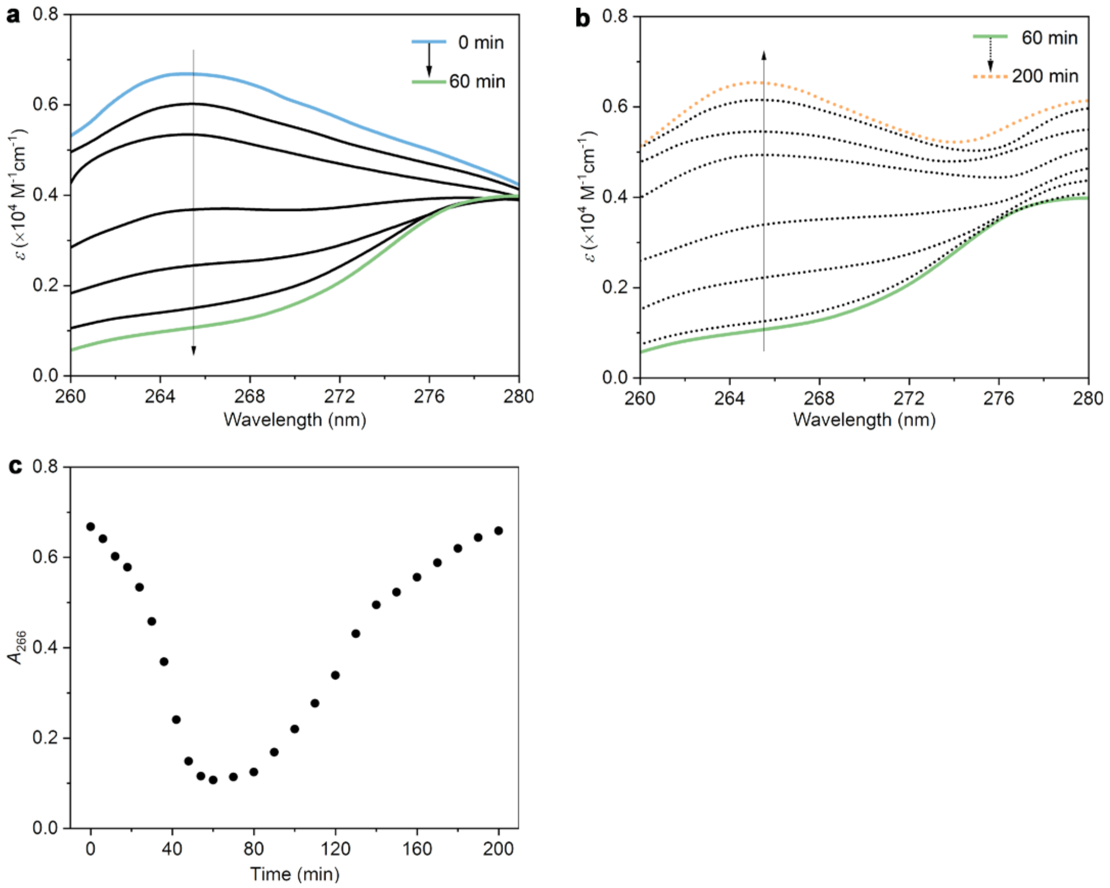

Figure S15. (a,b) UV-Vis spectral variation of FLP precursor (**C$_{11}$TP** and **TB**) and **S1** substrate upon addition of CO_2 over time: (a) 0~60 min and (b) 60~200 min. (c) The change in absorption intensity of FLP species at 266 nm as a function of time.

It is known that free FLP species has a characteristic absorption at 266 nm, thereby we could monitor the change of this absorption band (A_{266}) to determine the concentration of FLP in solution. In the first 60 min, this absorption gave a gradual decrease to near zero, indicating that almost all FLP units formed CO_2-bound structure (***Figure S15a***). However, in the next 140 min, this absorption showed a spontaneous increase back to the initial intensity, indicating a reverse debinding process existed in the system to consume CO_2-bound FLP units (***Figure S15b***). Based on Eq. 6 and the feed FLP is at C_0 = 1.0 mM, the apparent rate coefficient of gas binding (k_+^{app}) is determined to be 2.60×10^{-4} s^{-1}, while the rate coefficient of gas debinding (k_-^{app}) is 1.04×10^{-4} s^{-1}. It is clear that the forward reaction rate is as a factor of 2.5 than that of the backward rate. This kinetic asymmetry is crucial to maintaining a CO_2-driven transient gelation among FLP precursors and substrate.

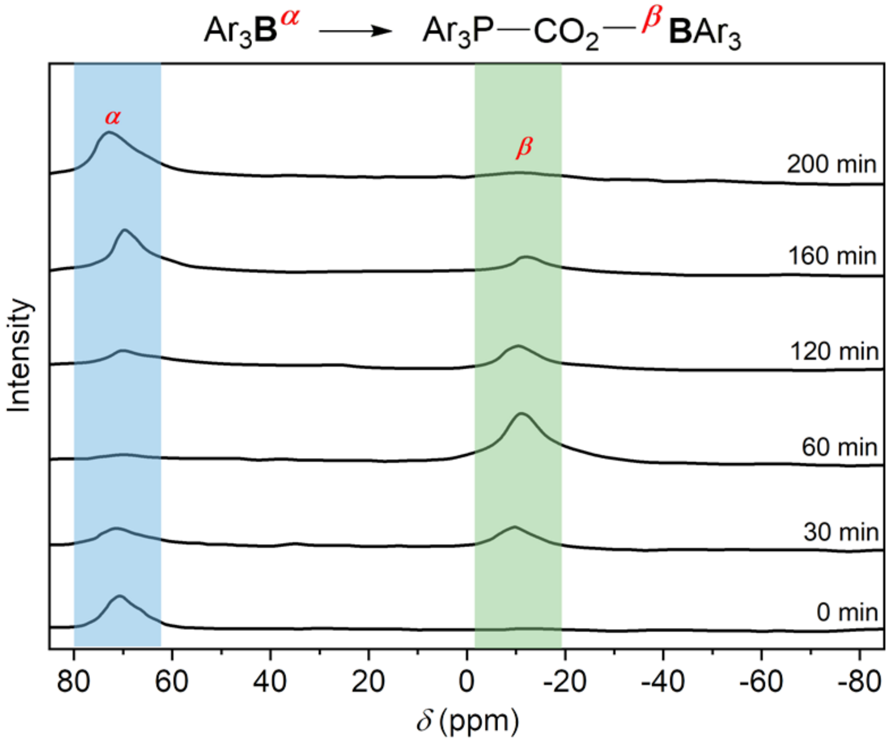

Figure S16. ^{11}B NMR spectral change of FLP precursors and **S1** upon addition of CO_2 over time (0–200 min).

At the beginning (0 min), the solution showed typically single, broad ^{11}B signal around δ = 70 ppm (B^{α}), assigned to the three-coordinated triarylborane (**TB**) species. However, after CO_2 treatment, this signal was gradually depressed, whereas a new broad peak at δ = -10 ppm (B^{β}) appeared and enhanced within 60 min. This peak is ascribed to the four-coordinated borane, indicating the formation of P–CO_2–B bridging bond. In the next 140 min, a reversible recovery can be found, that is, B^{α} signal showed a gradual enhancement but B^{β} was weakened until back to the initial state. This indicates that the formed P–CO_2–B bridging linkages are spontaneously disconnected and return to the free FLP form [1].

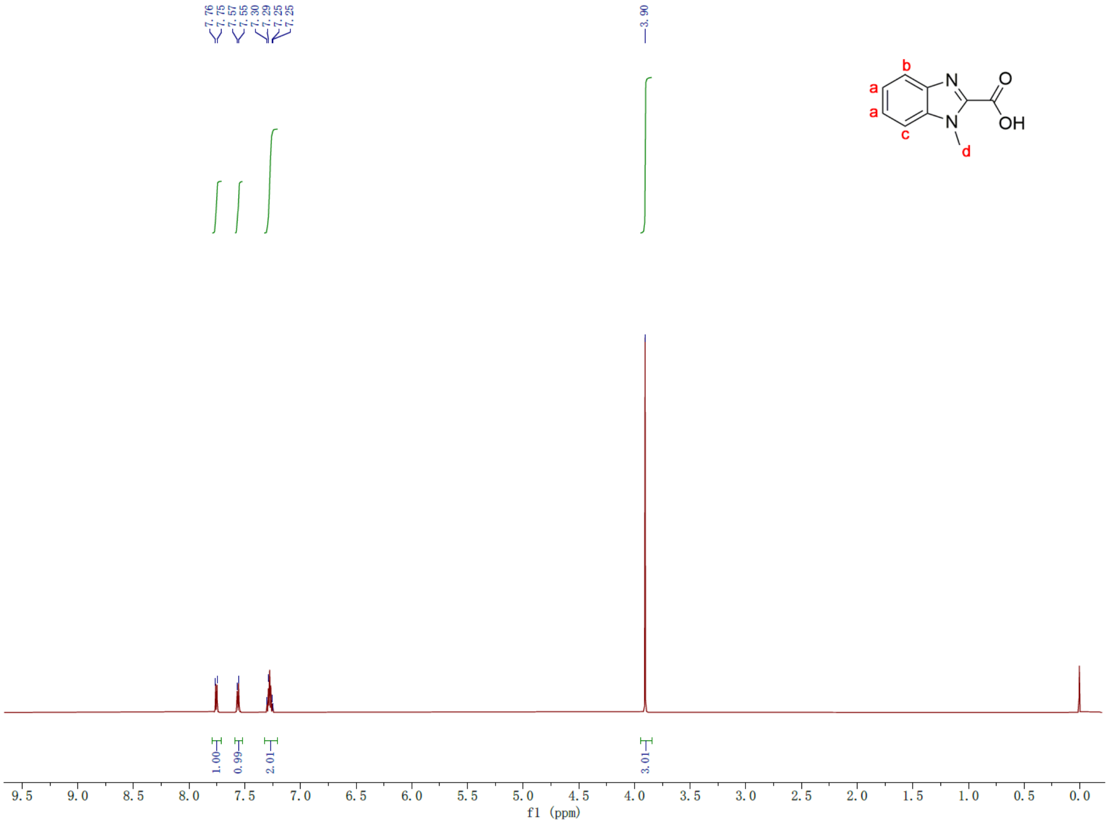

Figure S17. ^{1}H NMR spectrum of standard sample of benzo[d]imdiazole-2-carboxylic acid.

The standard sample of benzo[d]imdiazole-2-carboxylic acid is commercially available and used as received. Its typical ^{1}H NMR ($CDCl_3$) showed three groups of proton peaks at 7.76 ppm (1H, d), 7.55 (1H, d), 7.25 (2H, m), and 3.90 (3H, s). These signals are consistent well with the product from transient gel system.

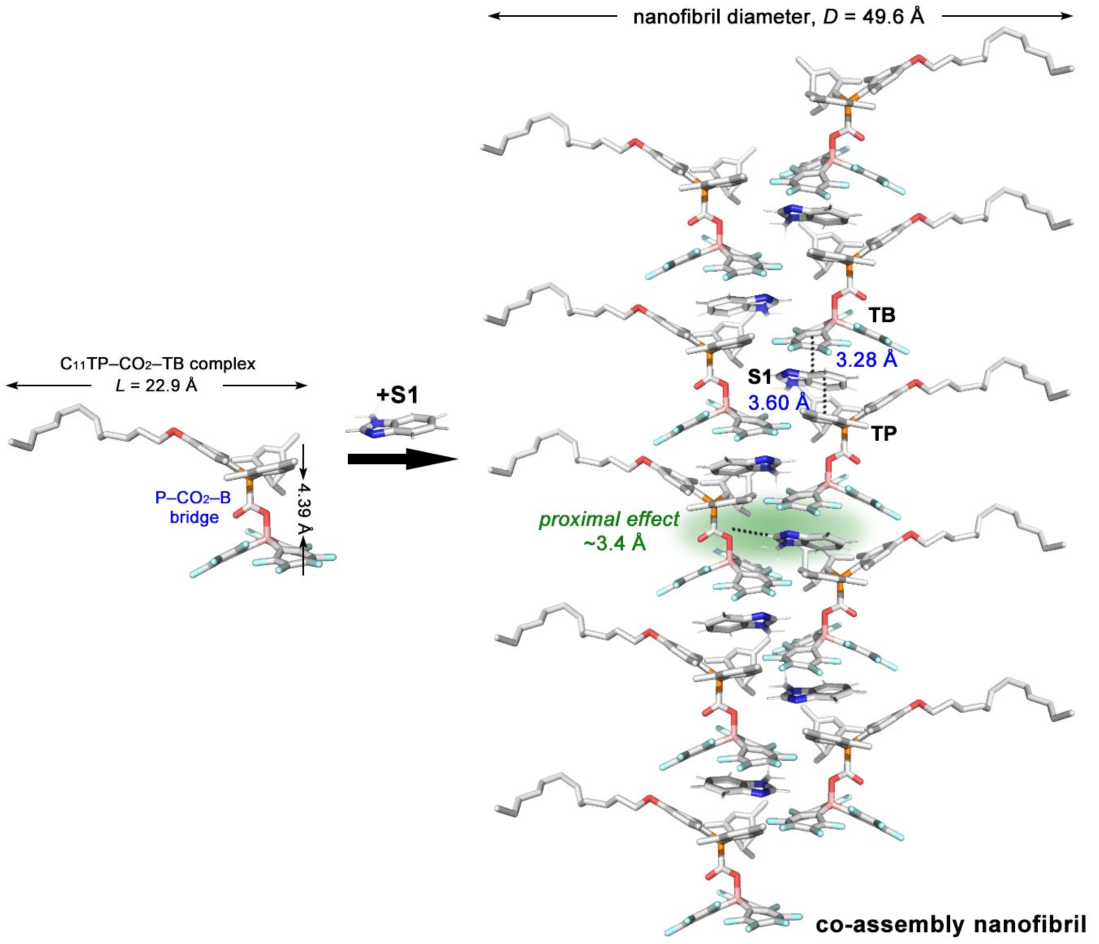

Figure S18. Molecular simulation of the co-assembly packing fashion of the CO_2-FLP complex and **S1** substrate into a nanofibril.

For an individual CO_2-FLP complex, it forms typical gas-bridged structure, in which CO_2 is bridged between the frustrated Lewis base **C_{11}TP** and frustrated Lewis acid **TB**, thus leading to a **C_{11}TP**–CO_2–**TB** dynamic complex. The optimized molecular length of this complex is 22.9 Å and the distance between boron and phosphorus center (P–CO_2–B bridge length) is determined to be 4.39 Å. When this **C_{11}TP**–CO_2–**TB** complex co-assembles with **S1** substrate, they are arranged in a 1D axial direction through the synergy of polar-π and π-π interactions, where **S1** moieties are sandwiched between the two complexes but is closer to **TB** (3.28 Å) than to the **TP** moiety (3.60 Å). Since **TB** unit is of multiple fluorine substituents, its strong electron-withdrawing ability makes it tightly bind with **S1** via polar-π interactions, while **TP** moiety can bind to **S1** through π-π interactions. Notably, because **S1** is closer to **TB** than to **TP**, it indicates that the contribution of polar-π interactions are larger than that of π-π interactions to govern this intermolecular co-assembly. On the other hand, the distance of **S1** and the adjacent CO_2-bridged bond within this arrangement is only ~3.4 Å. This would produce a proximal effect, which probably becomes the structural basis for the catalysis of substrate.

4. Supplementary characterization for periodic regulation of CO_2-fueled transient gelation.

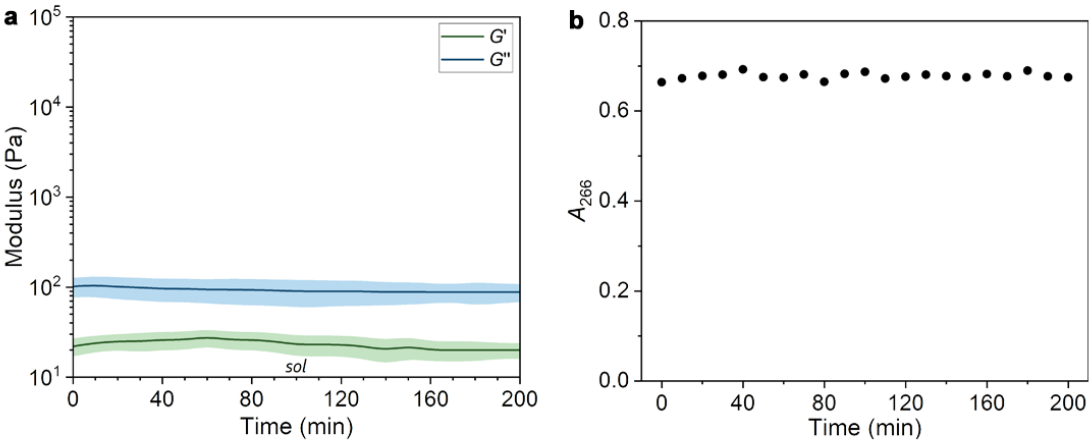

Figure S19. Control experiment using fluorine-free **TB^F** as precursor instead of **TB**: (a) Rheological monitoring and (b) UV-Vis spectral monitoring against time.

When we used **TB^F** as precursor to replace TB, the system remained in sol state all the time, as confirmed by $G'' > G'$ (***Figure S19a***). Moreover, no spectrometric change at 266 nm was seen (***Figure S19b***), indicating that the system has no catalytic activity.

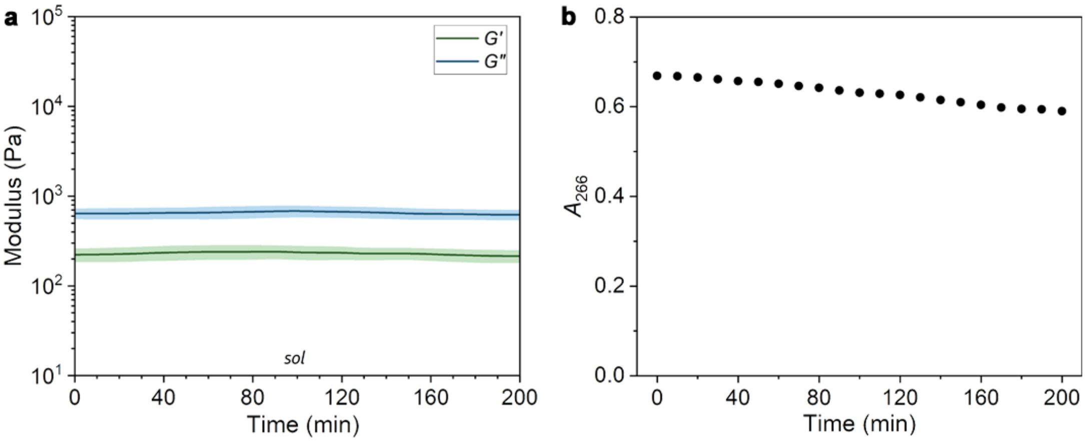

Figure S20. Control experiment using **SC** as substrate instead of **S1**. (a) Rheological monitoring and (b) UV-Vis spectral monitoring against time.

When we used **SC** as precursor to replace **S1**, the system remained in sol state all the time, as confirmed by $G'' > G'$(***Figure S20a***). But its storage modulus is estimated to be ~240 Pa, higher than the case of $\mathbf{TB^F}$ (<30 Pa), which indicates that **SC** as substrate can somewhat induce co-aggregation without ordered, regular aggregation. Moreover, the typical absorption at 266 nm showed a slight decrease (***Figure S20b***), which means that the system has neglected catalytic ability.

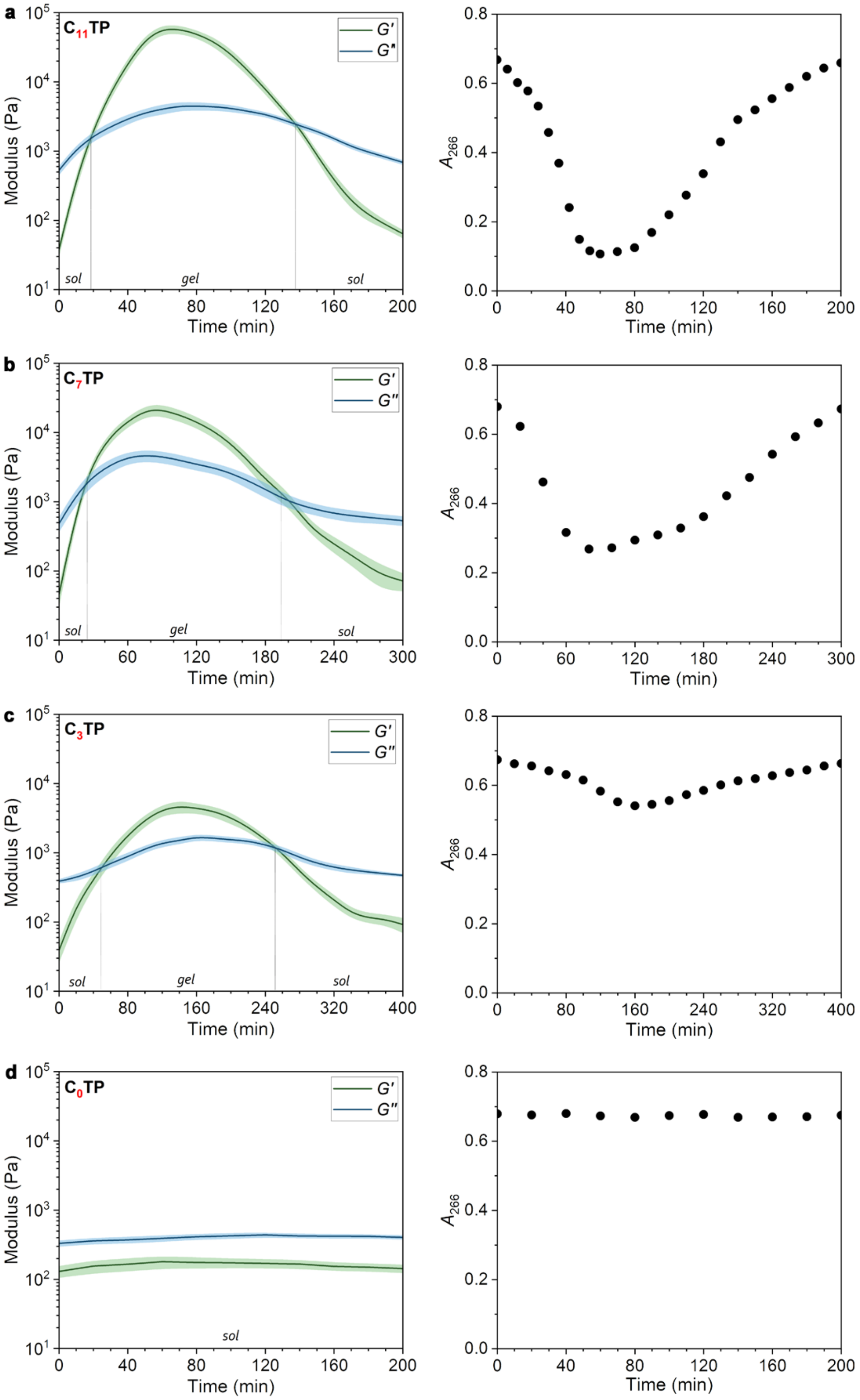

Figure S21. Control experiment using **C_nTP** as the Lewis basic precursor.

Rheological monitoring (left panels) and UV-Vis spectral monitoring against time (right panels) under different chain length: (a) n = 11, (b) n = 7, (c) n = 3, and (d) n = 0.

From ***Figure S21a-c***, it can be found that the shorter the alkyl chain installed on **TP** moiety was, the weaker the strength of formed transient gel showed. In comparison to **C_{11}TP** system (*G′* = 58.2 kPa), the gel modulus in the presence of **C_7TP** declined a half (*G′* = 22.8 kPa), while that in the case of **C_3TP** less than one-tenth of the original (*G′* = 4.7 kPa). Meanwhile, the reverse catalytic reaction encountered lessened activity with the decrease of Lewis base in solvophobicity. Notably, from ***Figure S21d***, if the alkyl tail was absent (**C_0TP**), it is unable to support the gelation because of no solvophobic effect to assist the intermolecular co-assembly process.

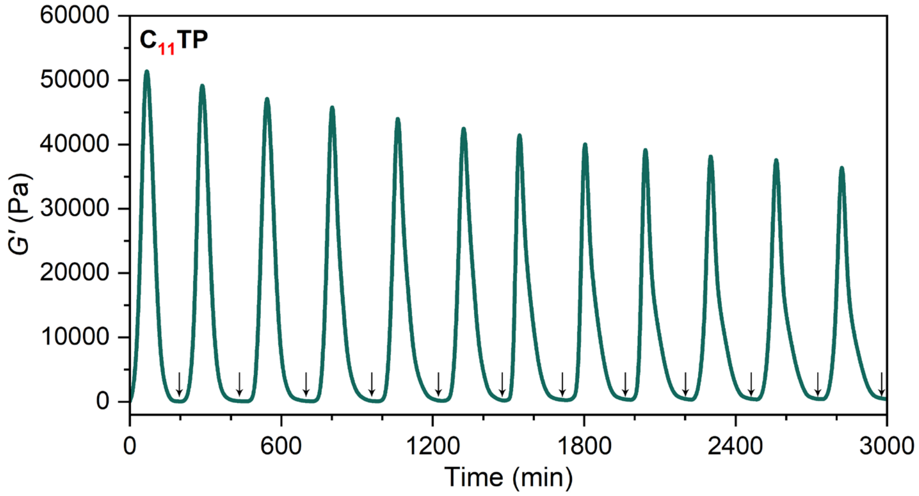

Figure S22. Tunable periodic behavior of CO_2-fueled transient gelation by regulating the internal and external factors. In this case, using **C_{11}TP** as the precursor. The arrows indicate the resupply of CO_2 fuel in batch-wise mode (1 mM).

It can be found that in the case of **C_{11}TP** such a transient gelation is reproducible for over 12 cycles upon addition CO_2 fuel in batch, and maintains a long-term lifespan of 3000 min with only 20% decay in gel strength. This shows their favorable periodicity, durability, and recyclability, which helps for subsequent functional applications.

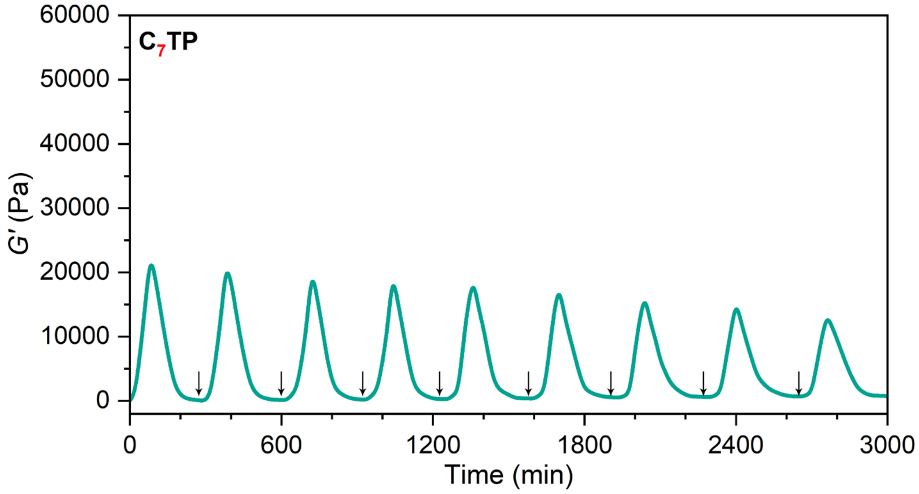

Figure S23. Tunable periodic behavior of CO_2-fueled transient gelation by regulating the internal and external factors. In this case, using **C_7TP** as the precursor. The arrows indicate the resupply of CO_2 fuel in batch-wise mode (1 mM).

As compared to **C_{11}TP**, the mechanical oscillating amplitude is attenuated (*G*' ~ 20 kPa) and the oscillation period becomes longer (~308 min).

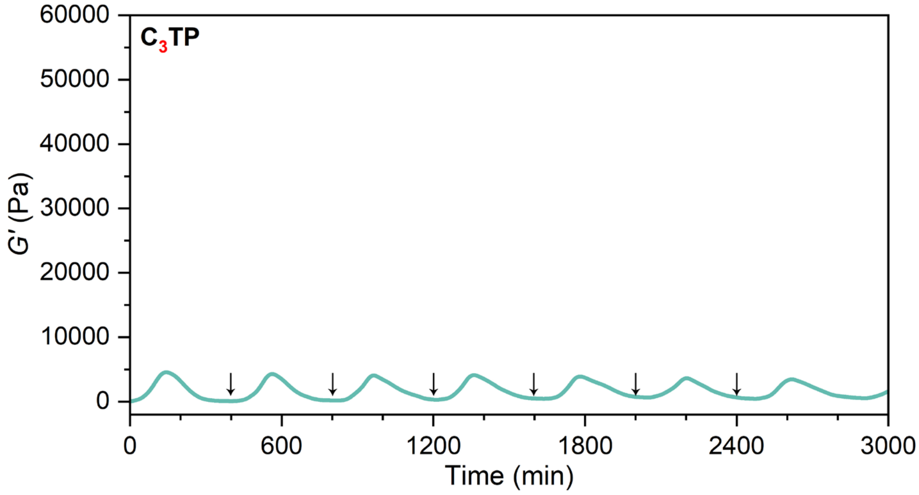

Figure S24. Tunable periodic behavior of CO_2-fueled transient gelation by regulating the internal and external factors. In this case, using **C_3TP** as the precursor. The arrows indicate the resupply of CO_2 fuel in batch-wise mode (1 mM).

As compared to **C_{11}TP**, the mechanical oscillating amplitude is further attenuated (*G*' ~ 4 kPa) and the oscillation period becomes much longer (~410 min).

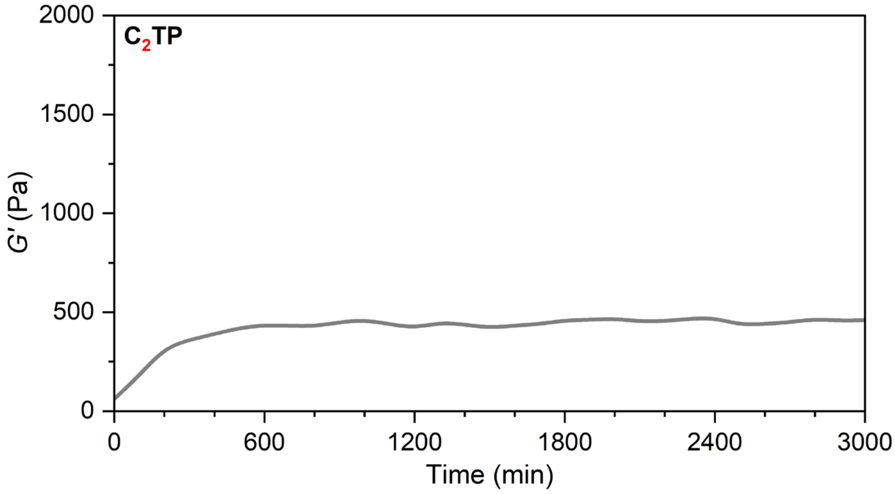

Figure S25. CO_2-fueled co-assembly system by using **C_2TP** as the precursor.

When the length of alkyl chain decreases to 2, no periodic gelation can be seen. As gas fuel was added, the solution rheology gave a bit ascent but kept constant, indicating a slight increase in sol viscosity. Such a chain length in TP precursor is considered as a critical point (n = 2) that can support the transient gelation and periodic phase transition.

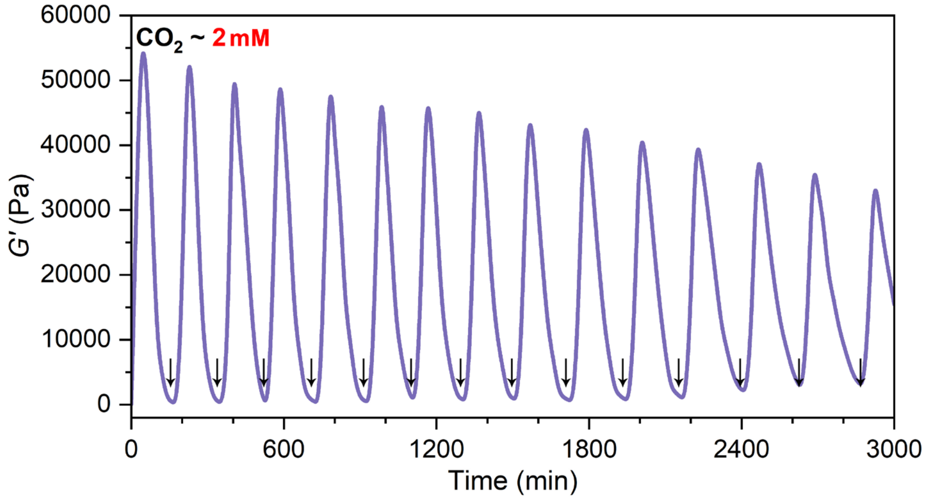

Figure S26. Tunable periodic behavior of CO$_2$-fueled transient gelation by regulating the factor of gas fuel concentration. In this case, CO$_2$ fuel level is at 2 mM (2 equiv.). The arrows indicate the resupply of CO$_2$ in batch-wise mode (2 mM in each addition).

As compared to the standard reference (CO$_2$ fuel level, 1 mM), the total period of one gelation cycle has a significant acceleration (~185 min), while the initial mechanical strength of formed gel is *G'* ~ 54 kPa, and show a 35% decay after 15 cycles.

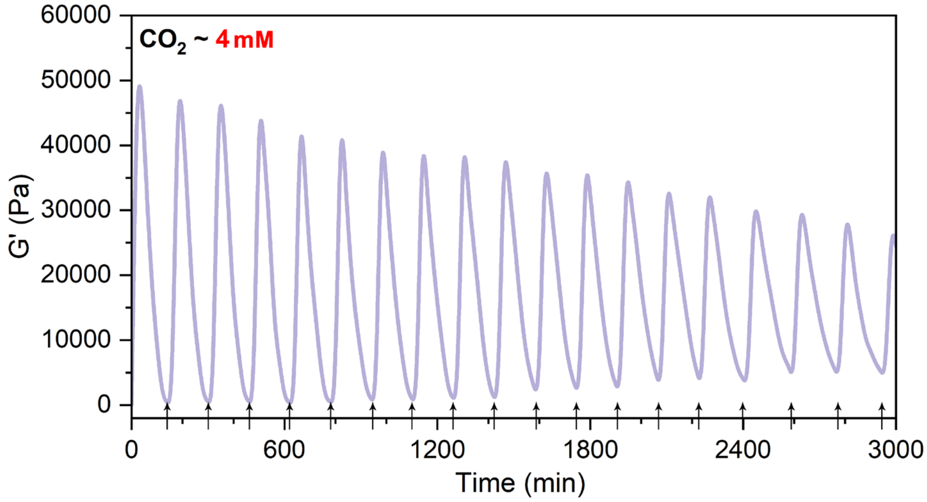

Figure S27. Tunable periodic behavior of CO$_2$-fueled transient gelation by regulating the factor of gas fuel concentration. In this case, CO$_2$ fuel level is at 4 mM (4 equiv.). The arrows indicate the resupply of CO$_2$ in batch-wise mode (4 mM in each addition).

As compared to the standard reference (CO$_2$ fuel level, 1 mM), the total period of one gelation cycle has a further acceleration (~156 min), while the initial gel mechanical strength slightly decreases to *G'* ~ 49 kPa, and show a 40% decay after 18 cycles.

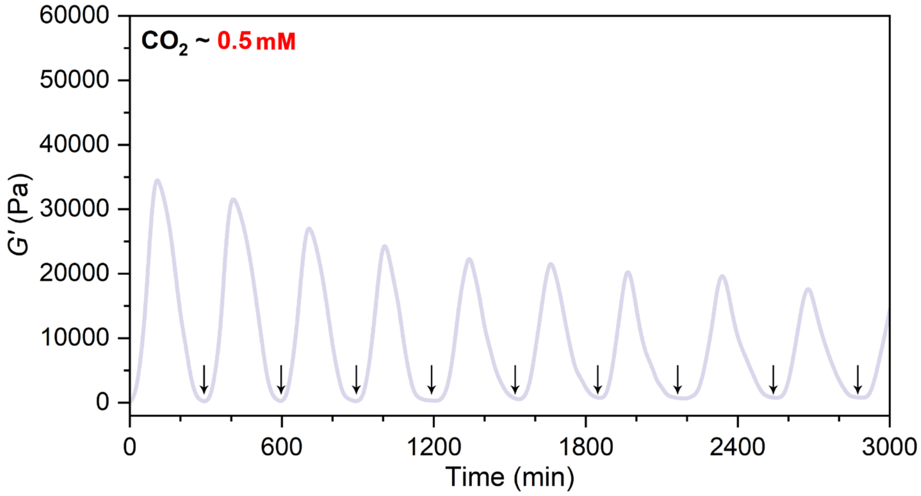

Figure S28. Tunable periodic behavior of CO_2-fueled transient gelation by regulating the factor of gas fuel concentration. In this case, CO_2 fuel level is at 0.5 mM (0.5 equiv.). The arrows indicate the resupply of CO_2 in batch-wise mode (0.5 mM in each addition).

As compared to the standard reference (CO_2 fuel level, 1 mM), when CO2 level is un-saturated, it results in a retard period (~300 min), while the initial mechanical strength of gel also drops significantly to *G'* ~ 34 kPa, and the modulus oscillation has a gradual attenuation in amplitude.

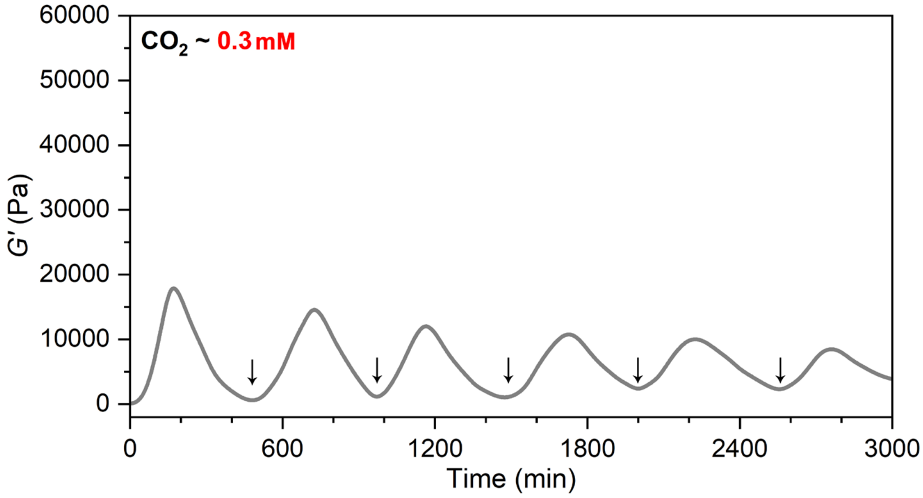

Figure S29. CO_2-fueled co-assembly system with 0.3 mM of fuel level.

When the concentration of gas fuel decreases to 0.3 mM in batch addition, it ekes out the periodic behavior of transient gelation; however, it is clear that the oscillation of gel mechanical strength has a gradual decay until complete loss of the change after 6 cycles. This indicates that the lowest critical point on fuel level is around 0.3 mM.

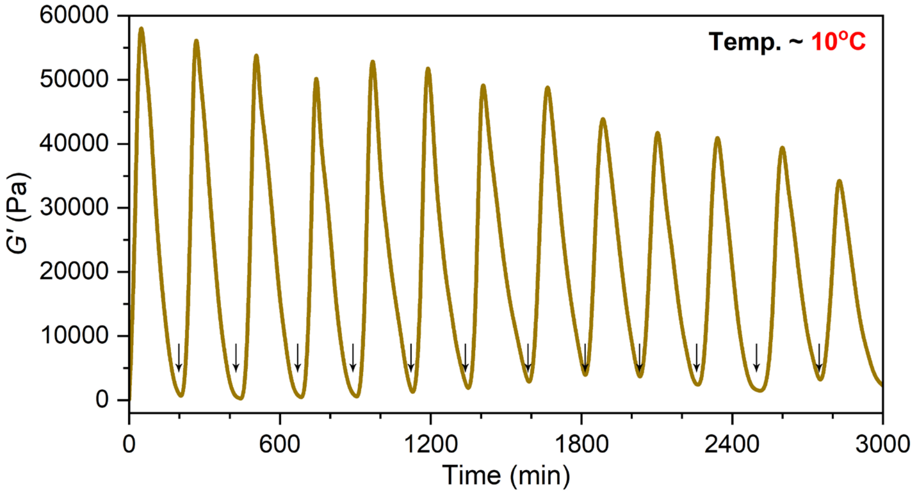

Figure S30. Tunable periodic behavior of CO_2-fueled transient gelation by regulating external temperature cue. In this case, temperature is fixed at 10 ºC. The arrows indicate the resupply of CO_2 in batch-wise mode (1 mM in each addition).

As compared to the standard reference (20 ºC), the total period of one gelation cycle has a slight acceleration (~220 min), while the initial mechanical strength of formed gel is basically unchanged at *G'* ~ 60 kPa and remain ~58% gel strength over 13 cycles.

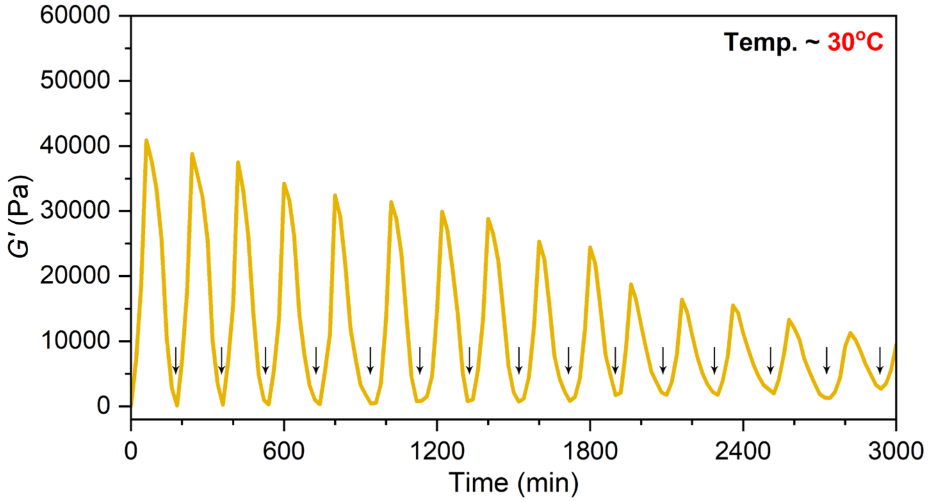

Figure S31. Tunable periodic behavior of CO_2-fueled transient gelation by regulating external temperature cue. In this case, temperature is fixed at 30 ºC. The arrows indicate the resupply of CO_2 in batch-wise mode (1 mM in each addition).

As compared to the standard reference (20 °C), the total period of one gelation cycle has a small drop and attains 190 min, but higher temperature is against gel mechanics. Its maximal modulus is only 40 kPa and declined by 80% after 15 cycles.

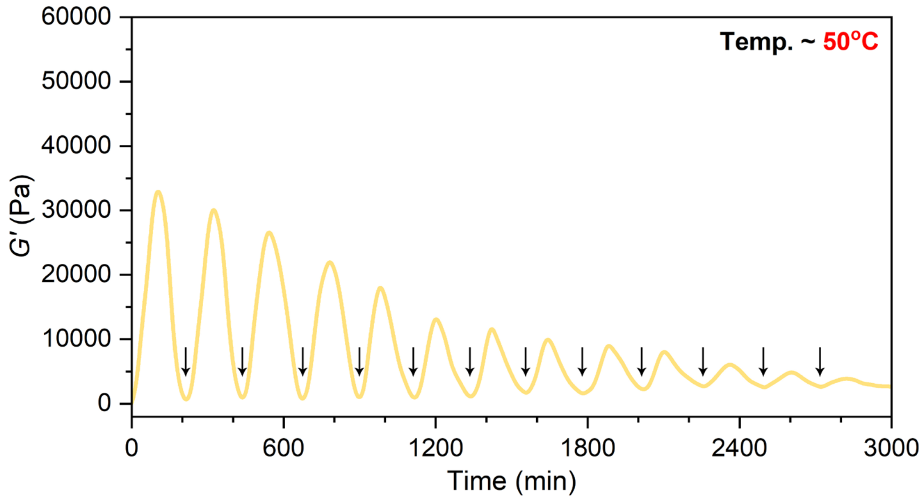

Figure S32. Tunable periodic behavior of CO_2-fueled transient gelation by regulating external temperature cue. In this case, temperature is fixed at 50 ºC. The arrows indicate the resupply of CO_2 in batch-wise mode (1 mM in each addition).

As compared to the standard reference (20 °C), the total period of one gelation cycle is nearly unchanged, whereas the initial gel modulus falls by half to ~33 kPa. Moreover, the oscillatory amplitude shows a rapid and large attenuation.

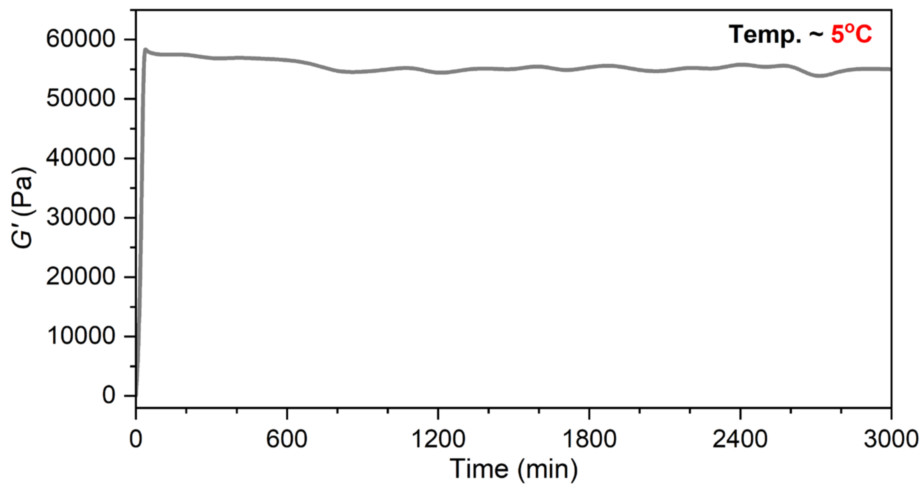

Figure S33. CO_2-fueled co-assembly system at the low temperature limit of 5 ºC.

As temperature is decreased to 5 ºC, the low temperature is favor of the forward gas-binding reaction, but highly inhibits the backward catalytic process. Thus, CO_2 gas can boost the gel formation (*G'* ~ 34 kPa), whereas the automated gel collapse cannot occur, which makes a permanent bulk gel (>3000 min). It suggests that such transient gelation exists a lower critical temperature threshold (~5 °C), below which no energy dissipation proceeds.

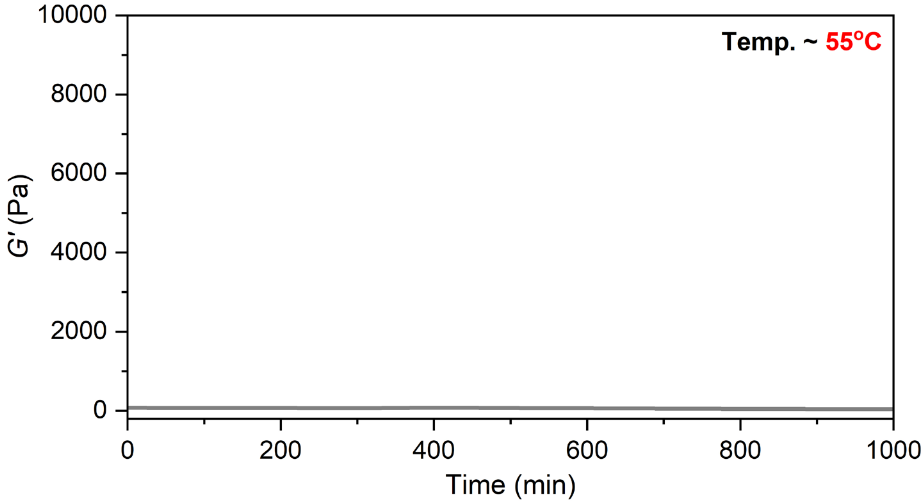

Figure S34. CO_2-fueled co-assembly system at the upper temperature limit of 55 °C.

As temperature is elevated to 55 °C, the high temperature totally prohibits the forward gas binding process. Consequently, no gel can form in this condition, and this indicates that an upper temperature limit (~55 °C) exists in this co-assembly system, above which the transient gelation and CO_2-fueled periodic behavior is not permitted.

Table S1. Comparison of diverse categories of substrates.

Substrate	Diverse categories	Gel lifecycle	Reactivity
SC	weak aromaticity	no gel	weak aromaticity and less electronic delocalization
S1-S5	benzoxazole-type	160-238 min	moderate acidity of C-H bond
S6-S9	quinoline-type	350~700 min	lower acidity of C-H bond
S10-S12	quinazoline-type	~152 min	higher acidity of C-H bond

5. Supplementary data for the application of transient gel materials.

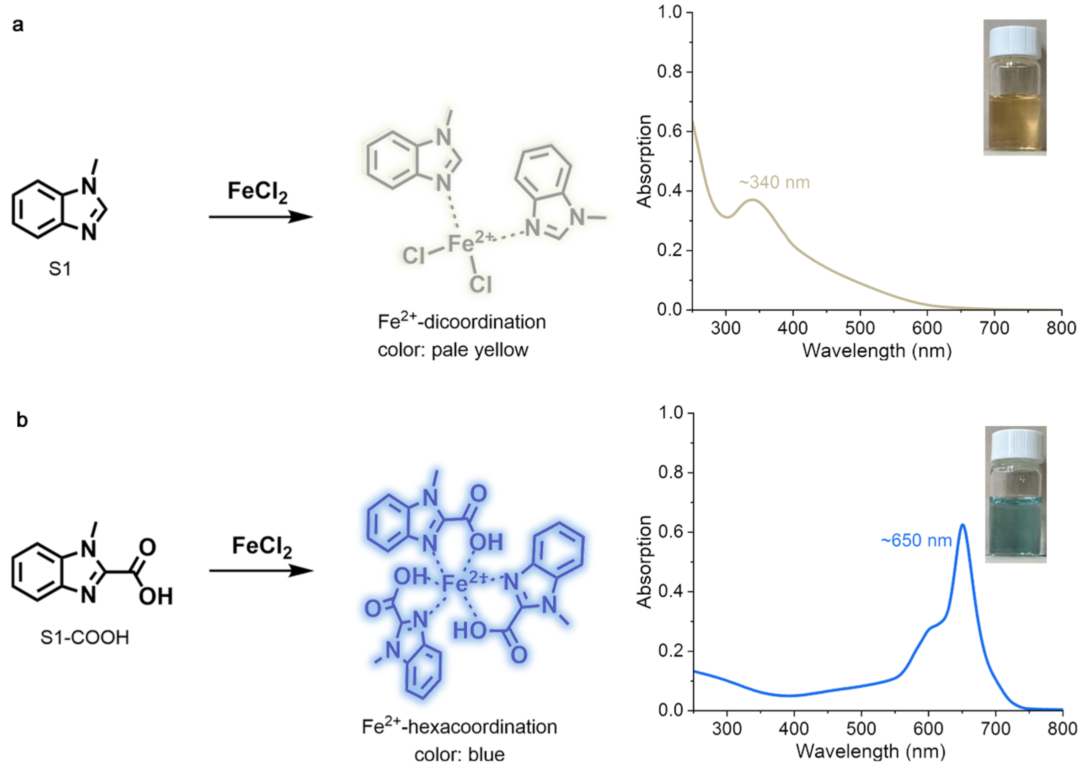

Figure S35. Using the difference on coordination structures and diagnostic color effects of Fe^{2+} ion with the *N*-methyl benzimidazole (**S1** substrate) and the product *N*-methyl benzimidazole carboxylic acid (S1-COOH product) to distinguish the sol-gel transition time: a) **S1** substrate can form a weak di-coordination complex with Fe^{2+} ion and show pale yellow color (UV-vis absorption at the wavelength of ~340 nm), b) S1-COOH product can form a strong hexa-coordinated complex with Fe^{2+} ion and show blue color (UV-vis absorption at the wavelength of ~650 nm) [9].

Reference

1 Chen L, Liu RJ, Hao X, Yan Q. *Angew Chem Int Ed,* **2019**, *58*: 264-268

2 Takeda Y, Nishida T, Minakata S. *Chem Eur J,* **2014**, *20*: 10266-10270

3 Campos J, Espada MF, López-Serrano J, Carmona E. *Inorg Chem,* **2013**, *52*: 6694-6704

4 Dankwardt JW. *Angew Chem Int Ed,* **2004**, *43*: 2428-2432

5 Pal S, Reja A, Bal S, Tikader B, Das D. *Angew Chem Int Ed,* **2022**, *61*: e20211857

6 Usov I, Mezzenga R. *Macromolecules,* **2015**, *48*: 1269-1280

7 Bal S, Das K, Ahmed S, Das D. *Angew Chem Int Ed,* **2018**, *58*: 244-247

8 Ahmed S, Chatterjee A, Das K, Das D. *Chem Sci,* **2019**, *10*: 7574-7578

9 Nandanwar SK, Borkar SB, Wijaya BN, Cho JH, Tarte NH, Kim HJ, *Biol Chem Chem Biol,* **2020**, *5*: 3471-3476